

## RESEARCH ARTICLE

## Isolation and transcriptional characterization of mouse perivascular astrocytes

Nejla Yosef<sup>1</sup>, Yuanxin Xi<sup>2</sup>, Joseph H. McCarty<sup>1\*</sup>

**1** Department of Neurosurgery, University of Texas M.D. Anderson Cancer Center, Houston, TX, United States of America, **2** Department of Bioinformatics and Computational Biology, University of Texas M. D. Anderson Cancer Center, Houston, TX, United States of America

\* [jhmccarty@mdanderson.org](mailto:jhmccarty@mdanderson.org)

## Abstract

In the post-natal mammalian brain perivascular astrocytes (PAs) ensheath blood vessels to regulate their unique permeability properties known as the blood-brain barrier (BBB). Very little is known about PA-expressed genes and signaling pathways that mediate contact and communication with endothelial cells (ECs) to regulate BBB physiology. This is due, in part, to lack of suitable models to distinguish PAs from other astrocyte sub-populations in the brain. To decipher the unique biology of PAs, we used in vivo gene knock-in technology to fluorescently label these cells in the adult mouse brain followed by fractionation and quantitative single cell RNA sequencing. In addition, PAs and non-PAs were also distinguished with transgenic fluorescent reporters followed by gene expression comparisons using bulk RNA sequencing. These efforts have identified several genes and pathways in PAs with potential roles in contact and communication with brain ECs. These genes encode various extracellular matrix (ECM) proteins and adhesion receptors, secreted growth factors, and intracellular signaling enzymes. Collectively, our experimental data reveal a set of genes that are expressed in PAs with putative roles in BBB physiology.

## OPEN ACCESS

**Citation:** Yosef N, Xi Y, McCarty JH (2020) Isolation and transcriptional characterization of mouse perivascular astrocytes. PLoS ONE 15(10): e0240035. <https://doi.org/10.1371/journal.pone.0240035>

**Editor:** Ramani Ramchandran, Medical College of Wisconsin, UNITED STATES

**Received:** May 25, 2020

**Accepted:** September 17, 2020

**Published:** October 8, 2020

**Copyright:** © 2020 Yosef et al. This is an open access article distributed under the terms of the [Creative Commons Attribution License](https://creativecommons.org/licenses/by/4.0/), which permits unrestricted use, distribution, and reproduction in any medium, provided the original author and source are credited.

**Data Availability Statement:** All relevant data are within the manuscript and its Supporting Information files.

**Funding:** This work was supported by grants from the Cancer Prevention and Research Institute of Texas (RP180220), the National Institutes of Health (R01NS087635, R21NS103841, and P50CA127001), the Brockman Foundation, and the Terry L. Chandler Foundation. The funders had no role in study design, data collection and analysis, decision to publish, or preparation of the manuscript. Joseph McCarty received salary from

## Introduction

The blood-brain barrier (BBB) is formed and maintained through complex interactions between cells of the neurovascular unit (NVU), which is comprised of endothelial cells (ECs), pericytes, astrocytes, microglia and neurons [1, 2]. Various glial-derived pathways have been identified that promote the formation of the BBB during embryonic and neonatal development [3]. For example, vascular endothelial growth factor-A (VEGF) expressed by glial cells signals via the VEGFR2 receptor tyrosine kinase in ECs to control blood vessel sprouting and permeability [4]. In addition, Wnt growth factors secreted by glial cells promote angiogenesis and barrierogenesis [5] via  $\beta$ -catenin activation in ECs [6]. Wnt signaling also involves GPR124, an atypical G-protein coupled receptor expressed in ECs that is essential for vascularization [7, 8] via interactions with the Wnt co-receptor Reck [9]. Integrin-mediated activation of TGF $\beta$  signaling is also critically involved in control of angiogenesis and EC barrier development [10–13].

Astrocytes are an abundant cell type in the post-natal central nervous system (CNS) and have many important physiological functions at the NVU [14, 15]. In vitro models support

the Cancer Prevention and Research Institute of Texas (RP180220), the National Institutes of Health (R01NS087635, R21NS103841, and P50CA127001), the Brockman Foundation, and the Terry L. Chandler Foundation. Nejla Yosef received salary from the Brockman Foundation.

**Competing interests:** The authors have declared that no competing interests exist.

roles for mixed cultures of astrocytes in mediating the induction and maintenance of the BBB by controlling EC barrier characteristics including tight junction protein expression and trans-endothelial endocytosis [16]. However, astrocytes are highly heterogeneous and display variability related to differences in their lineage and regional location in the brain [17, 18]. Thus, most *in vitro* co-culture models likely lack accurate features involved in astrocyte contact and communication with ECs *in vivo*. PA end feet juxtapose nearly 80% of the abluminal surface of capillaries, revealing a crucial role for these cells in BBB physiology. Indeed, PA adhesion and signaling pathways are known to play important roles in regulation of the BBB. For example, the dystrophin-glycoprotein complex is enriched in PAs [19] and has roles in regulating BBB development and integrity [20]. Genetic deletion of the DGC component aquaporin 4 (*Aqp4*) in astrocytes leads to abnormal interactions with endothelial cells and impaired BBB integrity [21]. In addition, hedgehog produced by PAs is essential for normal control of BBB physiology via signaling through smoothed receptors in the vascular endothelium [22]. TGF $\beta$  signaling promotes expression of *Mfsd2a* in post-natal brain ECs [23]. *Mfsd2a* transports the omega-3 fatty acid docosahexaenoic acid (DHA) across the BBB and promotes BBB homeostasis, with genetic deletion of *Mfsd2a* in mice leading to BBB hyperpermeability and DHA deficiency [24, 25]. Loss-of-function mutations in human MFSD2A are linked to cognitive coordination impairment due to deficiencies in DHA metabolism [26]. In addition to these various EC-intrinsic signaling events, PAs also control blood vessel functions through communication with pericytes [27]. For example, pericyte interactions with ECs via the platelet derived growth factor B pathway is important for BBB integrity [28]. PAs also regulate brain homeostasis through modulation of the glymphatic system [29].

Additional mechanistic insights about how PAs regulate the BBB have been hindered by the lack of suitable *in vivo* models that distinguish PAs from other astroglial cell populations. Knock-in and transgenic strategies in mice commonly use promoters from glial fibrillary acidic protein (*Gfap*) [30], aldehyde dehydrogenase 1 family member L1 (*Aldh1l1*) [31], and glutamate aspartate transporter (*Slc1a3*) [32] genes to visualize and manipulate astrocytes. However, many of these models do not distinguish the diverse sub-populations of astrocytes found throughout the brain. Therefore, the selective identification, isolation and characterization of PAs is necessary for determining the full potential of PA-derived signaling pathways. In order to identify PA-expressed genes and pathways, we have focused efforts on the gene encoding megalencephalic leukoencephalopathy with subcortical cysts 1 (*Mlc1*), a transmembrane protein that is enriched in PA end feet [33]. Using T2A ribosome skipping strategies, we generated an mouse knock-in model in which the *Mlc1* gene drives the expression of enhanced green fluorescent protein (Mlc1-EGFP) [34] without perturbing expression of endogenous Mlc1 protein. Here, we have fractionated PAs from the brains of Mlc1-EGFP mice and analyzed their gene expression by quantitative single cell RNA sequencing. We also compared differential gene expression levels in PAs versus non-PAs and validated several of these genes as highly PA-enriched. Collectively, these data provide an important resource to the glial cell biology community and may reveal novel roles for PAs in the regulation of blood vessel functions, and particularly the BBB, in the adult brain.

## Materials and methods

### Experimental mice

This study was reviewed and approved by the MD Anderson Cancer Center Institutional Animal Care and Use Committee (IACUC) in compliance with the National Research Council Guide for the Care and Use of Laboratory Animals. The approved protocol number is ACUF-00001108-RN02. Mlc1-EGFP knock-in mice were generated as previously described [34].

Mlc1-EGFP/Mlc1-EGFP homozygous knock-in animals were crossed to homozygous GLAST-DsRed<sup>tg/tg</sup> transgenic mice [35] to generate Mlc1-EGFP<sup>+/+</sup>;GLAST-DsRed<sup>tg/+</sup> double heterozygous F1 progeny (Mlc1-EGFP<sup>+/+</sup>;GLAST-DsRed<sup>tg/+</sup>). All knock-in mice were on a mixed C57Bl6/129S1/FVB background. All animals were genotyped using PCR-based methodologies as reported previously [34, 35]. Mice were analyzed between postnatal day 30 (P30) and P90. We have reported previously that EGFP is stably expressed in perivascular astrocytes in the adult brain beyond P30 [34]. Since there were no reported sex-dependent differences in EGFP or DsRed expression in the two models, males and females were often combined for genomic or immunohistochemical analysis.

### scRNAseq experiments

Cerebral cortices were dissected from three adult Mlc1-EGFP<sup>+/+</sup> mice of similar age and placed in ice-cold PBS. In a tissue culture hood, cortices were minced using a sterile razor blade in a 60 mm petri dish containing sterile ice-cold 1X HBSS. After rapid transfer into a polypropylene tube, the suspension was centrifuged at 4°C and 300 g for 5 minutes. Cortical pellets were digested with an enzyme cocktail for 15 minutes using the Brain Tumor Dissociation Kit (#130-096-942) following the manufacturer guidelines (Miltenyi Biotec, Inc.). The suspension was gently mixed with a 5 ml pipette. The enzyme activity was terminated by addition of an equal volume of cold 1X HBSS. The suspension was gently mixed by pipetting several times with a 5 ml pipette and filtered through a 70 µm cell strainer into clean tubes to generate single cell suspensions. A live cell count was determined using the 0.4% trypan blue exclusion test, and enumeration was performed with a hemocytometer. Samples were centrifuged and resuspended with cold PBS containing 5% FBS at a concentration of 5x10<sup>6</sup> cells/ml. Samples were then transferred into polypropylene fluorescence-activated cell sorting (FACS) tubes for cell sorting by EGFP signal using a BD FACS Aria II cell sorter. GFP positive cells were sorted using a 100 µm nozzle and captured in a chilled tube containing PBS with 5% FBS. Fresh cell suspensions were immediately subjected to the scRNAseq protocol.

FAC-sorted PAs (EGFP<sup>+</sup> cells) from pooled cortices of three adult Mlc1-EGFP<sup>+/+</sup> mice were counted before being loaded onto the 10X Genomic Chromium instrument. The scRNAseq libraries were generated using the 10X Chromium Single Cell 3' v2 reagent kit and were sequenced on a Nextseq500 instrument. Sequencing data were analyzed using 10X Genomic Cell Ranger software. Expression matrices were processed by the SEURAT package v2.3.1 [36]. First, the raw UMI counts were normalized and scaled using the “NormalizeData” and “ScaleData” function in SEURAT. Principal component analysis was performed using highly variable identified by the “FindVariableGenes” function with default parameters, and significant principal components were selected to represent at least 80% of the total variance. Using these significant principle components, the UMAP plot was generated for two-dimensional visualization of multi-dimensional dataset. Clustering analyses were performed using the “FindCluster” function in SEURAT, with resolution set to 0.7 and reduction type set to “umap”. For each cluster, the marker genes were identified by comparing gene expression in the cluster vs other clusters, using Wilcoxon Rank-Sum test with adjusted p-value cutoff 0.05. To avoid sample size bias caused by different number of cells in each cluster, we sub sampled 50 cells from each cluster for the comparisons.

### Bulk RNAseq experiments

Cerebral cortices were dissected from the brains of adult Mlc1-EGFP;GLAST-DsRed mice (n = 4) of similar age (P30) in ice-cold PBS. Cerebral cortices from each mouse were dissociated separately into a single cell suspension as described above. A live cell count was

determined using the 0.4% trypan blue exclusion test, and enumeration was performed with a hemocytometer. Samples were centrifuged and resuspended with cold PBS at a concentration of  $5 \times 10^6$  cells/ml. Propidium iodide was added to suspensions prior to sorting to distinguish non-viable cells and cellular debris. Cell doublets were excluded from the sorted fractions by standard forward scatter and side scatter analyses. Gates for sorting PAs ( $EGFP^+;DsRed^+$ ) and non-PAs ( $DsRed^+$  cells) from *Mlc1-EGFP;GLAST-DsRed* double transgenic mice were determined using cell suspensions from *Mlc1-EGFP* or *GLAST-DsRed* cortical tissue. Samples were then transferred into FACS tubes for cell sorting by *DsRed* and *GFP* signals using a BD FACSAria II cell sorter. PAs ( $EGFP^+;DsRed^+$ ) and non-PAs ( $DsRed^+$  cells) were sorted using a 100  $\mu\text{m}$  nozzle and captured in a chilled tube containing PBS. Freshly sorted cell suspensions were immediately subjected to quantitative RNA sequencing to compare gene expression profiles. As gating controls for sorting, we used cells from dissociated cerebral cortices taken from adult *Mlc1-EGFP* mice and *GLAST-DsRed* mice.

FAC-sorted PAs ( $EGFP^+;DsRed^+$  cells) or non-PAs ( $DsRed^+$  cells) from mouse tissue ( $n = 4$  mice) were pelleted and the total RNA was extracted following the Qiagen RNeasy micro kit guidelines. After RNA quality was validated, eight samples of a RIN of  $\geq 7$  were loaded onto HiSeq400 instrument. Each astrocyte population was sequenced in quadruplicates. An average of  $\sim 43$  million paired-end reads were generated for each of the eight samples. Sequenced reads fastq files were mapped to mouse reference genome GRCm3 (mm10).using Tophat v2.0.13 [37]. Raw reads count were calculated using HTseq 0.12.4 [38]. Differentially expressed genes between  $EGFP^+;DsRed^+$  and  $DsRed^+$  cells were obtained with EdgeR package [39]. Differentially expressed genes are those having  $\log_2\text{FC} > 2$  and  $\text{FDR} < 0.01$ . Expression heat maps were generated using the differentially expressed genes. Volcano plots were generated using adjusted p-value (FDR) and  $\log_2$  fold changes. Gene set enrichment analysis was performed using the GSEA software [40]. The lists of enriched KEGG pathways were also compiled from GSEA results. For cross-referencing the PA 10 gene signature as well as 5 canonical astrocyte markers, we downloaded the normalized expression data matrix data for GSE72826 [18], and generated a heatmap showing relative expression levels of the selected genes. Hierarchical clustering analysis was performed to explore the expression patterns of these signature genes.

## Quantitative RT-PCR

Freshly sorted PAs ( $EGFP^+$  or  $EGFP^+;DsRed^+$  cells) and non-PAs ( $DsRed^+$  cells) were washed with cold PBS and the total RNA was extracted following the Qiagen RNeasy micro kit guidelines. RNA was reverse transcribed using Invitrogen SuperScript® III cDNA synthesis kit, and 100ng cDNA was used per reaction. qRT-PCR was carried out using Taqman primers, Taqman Universal Master Mix II on a StepOnePlus Real-Time PCR system (Applied Biosystems). The following Taqman qRT-PCR primers were used: Megalencephalic Leukoencephalopathy With Subcortical Cysts 1 (*Mlc1*, Mm00453827\_m1), Glial high affinity glutamate transporter (*Slc1a3*, Mm00600697\_m1), Aldehyde dehydrogenase 1 family member L1 (*Aldh1l1*, Mm03048957\_m1), Glial fibrillary acidic protein (GFAP, Mm01253033\_m1), Integrin subunit alpha-7 (*Itga7*, Mm00434400\_m1), laminin subunit alpha 5 (*Lama5*, Mm01222029\_m1), Semaphorin 4A (*Sema4a*, Mm00443140\_m1), Semaphorin 4B (*Sema4b*, Mm00803797\_m1), Four-jointed box protein 1 (*Fjx1*, Mm00487385\_s1), Growth differentiation factor 10 (*Gdf10*, Mm01220860\_m1), Gap junction beta-2 protein (*Gjb2*, Mm00433643\_s1), Follistatin-related protein 1 (*Fstl1*, Mm00433371\_m1), and Ectonucleoside triphosphate diphosphohydrolase 2 (*Entpd2*, Mm00515450\_m1). *18S* (4333760F) or *Gapdh* (Mm99999915\_g1) were used for normalization and relative gene expression ratios were calculated using quantitative  $\Delta\text{CT}$  methods.

Statistical analysis of qRT-PCR was performed using GraphPad prism 6 software. Differences between groups were analyzed using two-way analysis of variance (ANOVA) with Bonferroni post-hoc test and with the following denotations for statistical significance: \* $p < 0.05$ , \*\* $p < 0.01$ , \*\*\* $p < 0.001$ , \*\*\*\* $p < 0.0001$ .

### Immunofluorescence and confocal microscopy

Adult mice were anesthetized and fixed by cardiac perfusion with 4% paraformaldehyde (PFA) in PBS. Brains were removed and immersed in 4% PFA for 24 hours at 4°C. After fixation, brains were washed with cold 1XPBS 3 times for 10 minutes at 4°C. Then fixed brains were sagittally sectioned and embedded in 4% agarose. Then brains were sectioned at 100  $\mu\text{m}$  on a vibratome and stored in 1X PBS at 4°C. For immunofluorescence staining, sections were permeabilized and blocked with 1XTBS supplemented with 0.1% Triton-X and 10% donkey serum for 1 hour at room temperature (RT), followed by incubation with primary unconjugated antibodies diluted in the blocking solution and incubated overnight at 4°C. Immunofluorescence analyses were performed with the following primary antibodies: GFP, RFP, GFAP, and CD31 (S1 Table). These sections were then washed 3 times with TBS for 5 minutes and incubated with secondary antibodies (1:400 dilution), and 4'-6-Diamidino-2-phenylindole (DAPI) (1:500 dilution) in the blocking solution for 1 hour at RT (S1 Table). After washing with 1XTBS as previously stated sections were briefly washed with 1XPBS. Then sections were mounted on pre-treated microscope slides and sealed using vectashield (Vector Laboratories, Inc., Burlingame, Ca) mounting media and kept at 4°C until imaging. Confocal Images were acquired using an Olympus FLUOVIEW FV1000 20X and 40X objectives. All comparative images were taken with the same laser power and gain settings in order to make qualitative comparisons between staining levels in different samples. Multiple fields of view were imaged from biological replicates. The ratio of EGFP<sup>+</sup> cells, *DsRed*<sup>+</sup> cells or EGFP<sup>+</sup>/*DsRed*<sup>+</sup> cells was calculated with respect to total number of cells in a field of view. The total number of cells in the field of view was calculated by enumerating the number of DAPI stained nuclei using Adobe Photoshop CC (Adobe Systems, Inc.).

## Results

### Visualization of PAs in the cerebral cortex of Mlc1-EGFP mice

To characterize the molecular properties of brain PAs, we utilized the Mlc1-EGFP knock-in mouse model. In this model the *Mlc1* gene drives EGFP reporter expression via a T2A insertion without impacting endogenous Mlc1 protein expression [34]. Prior to fractionating -EGFP<sup>+</sup> cells from adult mice, we first confirmed the spatial distribution of EGFP<sup>+</sup> cells in the brain. The expression of EGFP in unfixed tissue was only weakly detected; therefore, we used an anti-GFP antibody in combination with an antibody directed against glial fibrillary acidic protein (GFAP) to reveal co-localization of EGFP and GFAP in astrocytes (Fig 1A–1C). These results are consistent with our prior report showing that EGFP<sup>+</sup> cells in Mlc1-EGFP mice express GFAP and are closely associated with brain blood vessels [34]. To selectively isolate and characterize PAs from the brain, cerebral cortices from adult Mlc1-EGFP mice were enzymatically digested and EGFP<sup>+</sup> cells were isolated using fluorescent activated cell-sorting (FACS) approaches. Despite the very low level of fluorescent signal detectable in fixed brain tissue slices, we detected EGFP by live cell sorting and successfully fractionated PAs from the cerebral cortices (Fig 1D). Thus, fluorescence-based sorting allows for the efficient identification and isolation of live PA cells from the adult Mlc1-EGFP mouse brain.

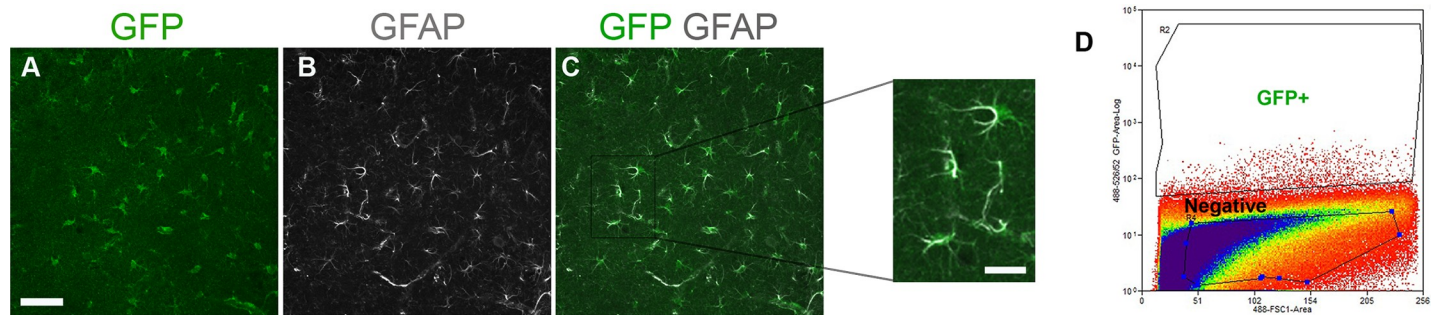


**Fig 1. Fractionation of PAs from the cerebral cortices of adult Mlc1-EGFP mice.** (A–C); Sagittal brain sections through the cerebral cortices of P30 mice were double immunolabeled with anti-GFP (A) and anti-GFAP (B) antibodies. Note the co-expression of GFP and GFAP in astrocytes (C). Scale bars, 50  $\mu$ m (A) and 10  $\mu$ m (inset, C). (D); Flow cytometric analyses of dissociated cerebral cortical cells from Mlc1-EGFP mice reveals that a low percentage of cells express EGFP (EGFP<sup>+</sup>). Note that the vast majority of cells do not express EGFP (Negative).

<https://doi.org/10.1371/journal.pone.0240035.g001>

## Single cell RNA sequencing analysis to identify genes with enriched expression in PAs

We next fractionated PAs from the cortices of adult Mlc1-EGFP mice (Fig 2A) followed by quantitative single cell RNA sequencing (scRNAseq). After computational comparisons, we performed graph-based clustering on all significant components. As a result, we detected seven distinct cell clusters, with the bulk of cells segregating into two main clusters with overlap due to similarities in mRNA expression (S1 Fig), although unbiased expression analyses of cell clusters 1 and 2 revealed some differences in gene expression (S2 Fig). The scRNAseq data were also visualized through a non-linear dimensional reduction algorithm (Fig 2B). Expression of well-established astrocyte transcripts such as *Mlc1*, *Slc1a3* and *Aldh11l* (Fig 2C) supported the astrocytic identity of PA fractions. In contrast, established markers for brain vascular ECs such as *Cldn5* were expressed at low or undetectable levels in clusters 1 and 2 (S3 Fig). Importantly, the scRNAseq data showed that PAs, and especially clusters 1 and 2, were enriched in mRNAs with published roles in vascular biology (S3 Fig). These enriched genes encode integrin beta8 (*Itgb8*) which activates TGF $\beta$  signaling in brain vascular endothelial cells [41] and vascular endothelial growth factor-A (*Vegfa*), which is expressed by astrocytes and regulates blood vessel permeability in the brain [42]. The top 20 most enriched genes in

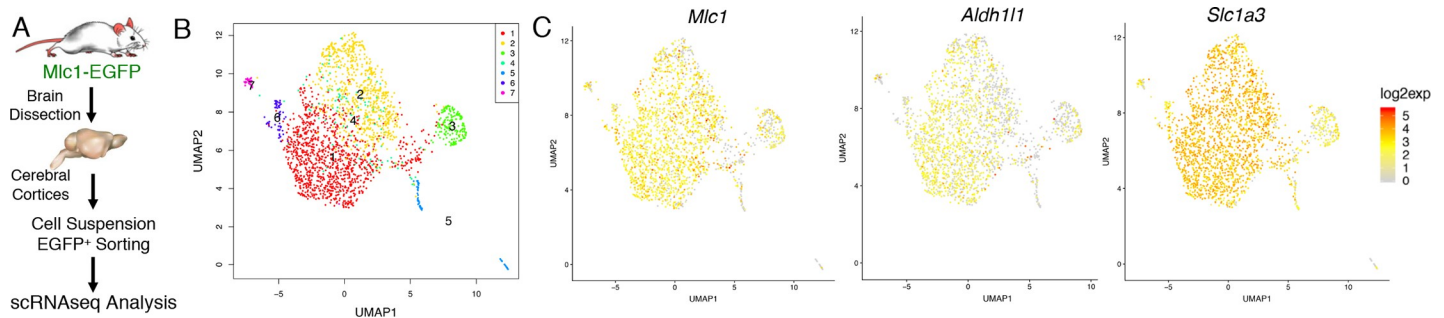


**Fig 2. Analysis of gene expression in PAs isolated from the cerebral cortices of adult Mlc1-EGFP mice.** (A); Schematic summarizing the experimental strategies for isolating cells from cerebral cortices of adult (P30) Mlc1-EGFP knock-in mice. Brain tissue was dissociated and live PAs were fractionated based on EGFP expression using FACS-based approaches. Single cells were subsequently analyzed using quantitative RNA sequencing. (B); Unsupervised clustering of single cell RNA sequencing data using EGFP-expressing PA cells fractionated from mouse cerebral cortices. Cells are clustered based on shared similarities in mRNA expression, with each of the two main clusters representing a subpopulation of PAs showing differential, but somewhat overlapping gene expression. (C); Feature plots showing the expression of select genes with established roles in mouse brain astrocytes including *Mlc1*, *Aldh11l*, and *Slc1a3*. Each dot indicates a distinct mRNA sequencing result from a single cell. Red indicates higher gene expression and grey indicates lower gene expression.

<https://doi.org/10.1371/journal.pone.0240035.g002>

each of the 7 isolated cell clusters are summarized in the Supplemental Materials section (S2–S8 Tables).

### Analyzing gene expression profiles in PAs versus non-PAs by RNAseq

To compare the gene expression profiles of PAs versus other astrocyte populations (non-PAs) in the brain that do not express Mlc1, we interbred Mlc1-EGFP homozygous knock-in mice with GLAST-DsRed transgenic mice [35] to generate Mlc1-EGFP;GLAST-DsRed F1 progeny. As detailed above, PAs express EGFP in the Mlc1-EGFP brain, whereas GLAST-DsRed transgenic mice express DsRed in many subsets of astrocytes, including PAs, throughout the brain via the astrocyte specific glutamate transporter (*Slc1a3*) promoter [35]. To confirm the astrocyte-specific expression patterns of EGFP and DsRed, we first labeled brain sections with antibodies recognizing GFP to identify PAs and RFP to identify PAs and non-PAs. In addition, anti-CD31 or anti-GFAP antibodies were included to identify vascular ECs or astrocytes, respectively. Our data showed that EGFP<sup>+</sup> and DsRed<sup>+</sup> single positive cells as well as double positive (EGFP<sup>+</sup>/DsRed<sup>+</sup>) cells were found throughout the cortex, cerebellum and hippocampus (Fig 3A–3C, 3F–3H and 3K–3M). Importantly, cells adjacent to blood vessels showed

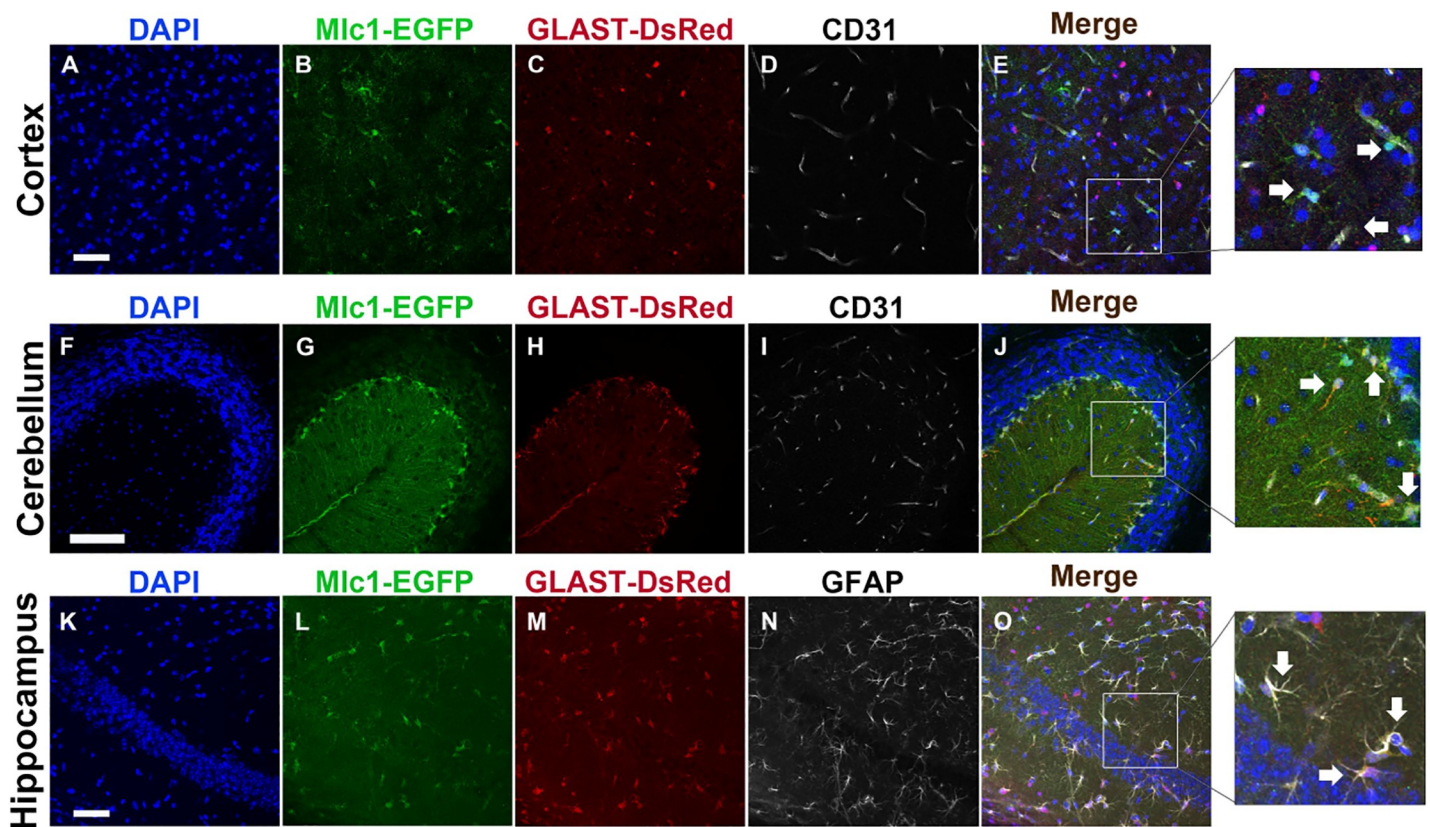


**Fig 3. Analyzing PA and non-PA cell distribution in adult Mlc1-EGFP;GLAST-DsRed mice based on EGFP and DsRed reporter expression.** (A–E); Coronal brain sections through the cerebral cortices of an adult Mlc1-EGFP; GLAST-DsRed mouse brain were labeled with DAPI (A), anti-GFP to detect PAs (B), anti-RFP to detect DsRed-expressing PAs and non-PAs (C), and anti-CD31 to detect vascular ECs that comprise blood vessels (D). Note that cells adjacent to cortical blood vessels (PAs) co-express GFP and DsRed (arrows in E), whereas DsRed<sup>+</sup> cells (non-PAs) that are more distal to CD31<sup>+</sup> ECs lack GFP expression. Scale bars, 100  $\mu$ m (A) and 20  $\mu$ m (inset, E). (F–J); Coronal sections through the cerebellum of an adult Mlc1-EGFP;GLAST-DsRed mouse brain stained with DAPI (F), anti-GFP (G), anti-RFP (H), and anti-CD31 (I). Note that most if not all cerebellar Bergmann glial cells, which are a radial glial-like astrocyte sub-population, co-express GFP and DsRed (arrows in J). Scale bars, 100  $\mu$ m (E) and 20  $\mu$ m (inset, J). (K–O); Coronal sections through the hippocampus of an adult Mlc1-EGFP;GLAST-DsRed mouse brain labeled with DAPI (K), anti-GFP (L), anti-RFP (M), and anti-GFAP (N). Note that many hippocampal astrocytes co-express GFP, DsRed, and GFAP (arrows in O). Scale bars, 100  $\mu$ m (K) and 20  $\mu$ m (inset, O).

<https://doi.org/10.1371/journal.pone.0240035.g003>

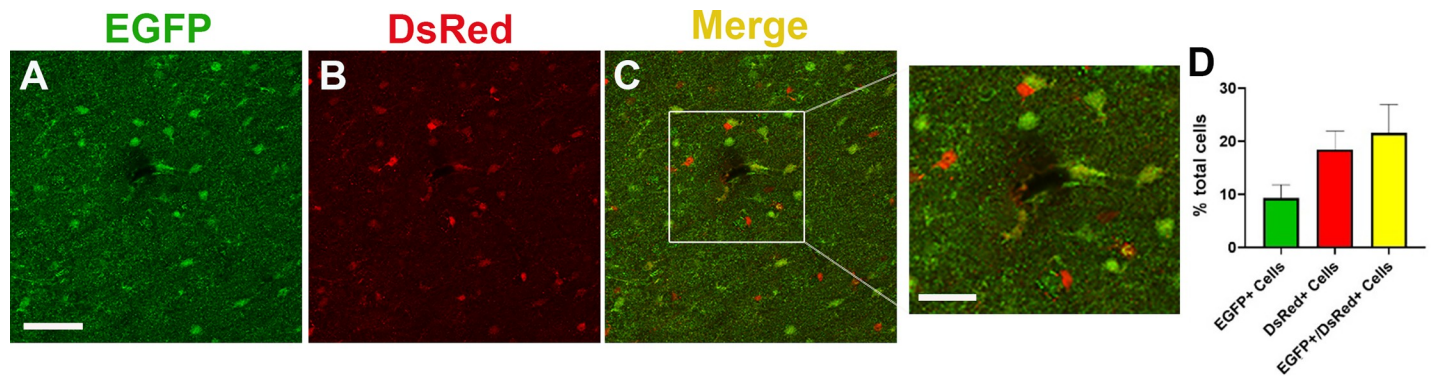


**Fig 4. Quantitation of PAs and non-PAs within the cerebral cortices of Mlc1-EGFP;GLAST-DsRed adult mice.** (A-C); Coronal brain sections through the cerebral cortices of adult Mlc1-EGFP;GLAST-DsRed mice were immunolabeled with anti-GFP antibodies (A) to visualize Mlc1-expressing cells (PAs) and anti-RFP antibodies (B) to visualize cells expressing DsRed via the *Slc1a3* promoter (PAs and non-PAs). In the merged confocal image (C), note that some cells express both EGFP<sup>+</sup> and DsRed<sup>+</sup>, whereas other cells are single positive for each fluorescent marker. Scale bar, 50  $\mu$ m (A) and 10  $\mu$ m (inset, C). (D); Quantification of the EGFP<sup>+</sup> and RFP<sup>+</sup> single positive cells as well as EGFP<sup>+</sup>/RFP<sup>+</sup> double positive cells in the cortices of Mlc1-EGFP;GLAST-DsRed mice. Numbers of fluorescence positive cells are plotted as a percentage of total numbers of cells based on DAPI labeling, although DAPI images have not been included in this figure. Note that more than 20% of cells within the adult cerebral cortex are EGFP<sup>+</sup> or EGFP<sup>+</sup>/RFP<sup>+</sup>, whereas non-PAs constitute approximately 20% or more of total cells. The red bars indicate DsRed<sup>+</sup>/EGFP<sup>+</sup> cell fractions.

<https://doi.org/10.1371/journal.pone.0240035.g004>

EGFP and DsRed co-expression, that were distinct from CD31 expressing vascular ECs (Fig 3D, 3E, 3I and 3J). Additionally, most cells showing co-expression of EGFP and DsRed were also positive for GFAP (Fig 3N and 3O). To more precisely determine the distribution of PAs and non-PAs in the cerebral cortex, we analyzed Mlc1-EGFP;GLAST-DsRed brain sections by immunolabeling with anti-GFP and anti-DsRed antibodies (Fig 4A–4C). Quantitation of the GFP, DsRed, and GFP/DsRed positive cells revealed that <10% were EGFP<sup>+</sup>, ~18% were DsRed<sup>+</sup>, and ~20% were EGFP<sup>+</sup>/DsRed<sup>+</sup> (Fig 4D).

To isolate sub-populations of PAs (EGFP<sup>+</sup>/DsRed<sup>+</sup>) and non-PAs (DsRed<sup>+</sup>) for gene expression comparisons, cerebral cortices from adult Mlc1-EGFP;GLAST-DsRed animals (n = 4) were dissociated. EGFP<sup>+</sup>/DsRed<sup>+</sup> double positive cells (PAs) and DsRed<sup>+</sup> single positive cells (non-PAs) were then fractionated by FACS (Fig 5A and 5B). Cortical cell suspensions prepared from Mlc1-EGFP or GLAST-DsRed single transgenic mice were used to control for gating by FACS (S4 Fig). Quantitative RNA sequencing comparisons (n = 4 mice) were performed using these two main cell populations. These data reveal that PAs express a unique set of genes that are not expressed at similar levels in the non-PA populations (Fig 5C and S5 Fig). Using this RNAseq data, we performed unsupervised gene set enrichment analysis for all the Kyoto Encyclopedia of Genes and Genomes (KEGG) pathways. We found that multiple signaling pathways were enriched in PAs, including ones involved in epithelial to mesenchymal transition, hedgehog signaling, and angiogenesis (S9 Table). Several differentially expressed genes identified in PAs encode proteins with links to extracellular matrix adhesion and signaling pathways. These genes include *Itga7*, *Lama3*, *Lama5*, *Frem1*, and *Frem2*. Additional genes were also identified with roles in cell-cell contact and communication including *Sema4a*, *Sema4b*, *Gdf10*, and *Gjb2* (Fig 5D and S10 Table). The 50 most highly enriched genes in the non-PA cell fractions (de-enriched in the PA fractions) are shown in S11 Table. A table containing numerical details, including p-values and average fold change for all genes analyzed in PAs versus non-PA fractions is also provided (S12 Table).

Consistent with the RNAseq data, qRT-PCR validation showed elevated levels of mRNAs in PAs as compared to non-PAs (Fig 5E). Correlation analyses between bulk RNAseq samples and scRNAseq data (clusters 1 and 2 in Fig 2) revealed that PAs (EGFP<sup>+</sup>/DsRed<sup>+</sup>) isolated from Mlc1-EGFP;GLAST-DsRed mice showed similar gene expression patterns with EGFP<sup>+</sup>



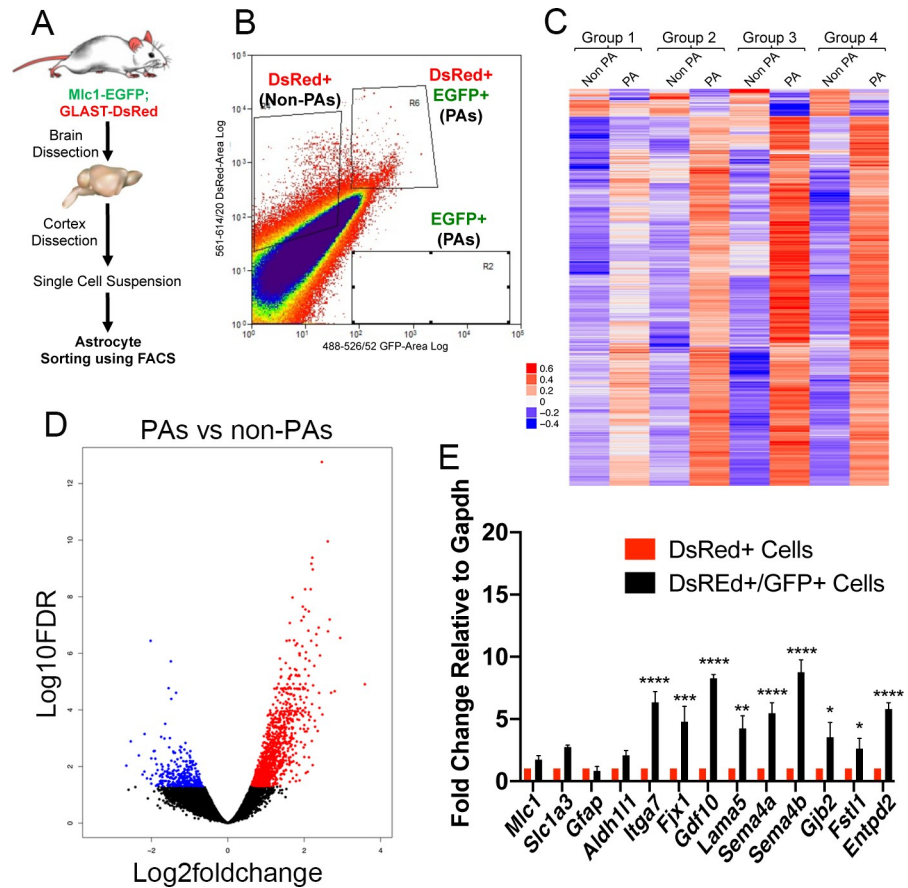


**Fig 5. Quantitative RNA sequencing to identify differentially expressed genes in PAs versus non-PAs isolated from Mlc1-EGFP;GLAST-DsRed adult mice.** (A); Strategy for dissection and analysis of cells from cerebral cortices of Mlc1-EGFP;GLAST-DsRed adult mice. Non-PAs (DsRed<sup>+</sup> cells) and PAs (EGFP<sup>+</sup>/DsRed<sup>+</sup> cells) were fractionated using FAC-based sorting approaches followed by comparative RNA sequencing. (B); Flow cytometry plot showing the profile of sorted DsRed<sup>+</sup> single positive cells (non-PAs) and EGFP<sup>+</sup>/DsRed<sup>+</sup> double positive cells (PAs) from the cerebral cortices. Note that the majority of cells are DsRed<sup>+</sup> and nearly all EGFP<sup>+</sup> cells are double positive for DsRed. The few cells in the lower box are EGFP<sup>+</sup> single positive PAs that lack DsRed expression. (C, D); Quantitative RNA sequencing comparisons reveal differentially expressed genes in PAs versus non-PAs as revealed by a color-coded heat map (C) and a volcano plot (D). Red indicates higher mRNA expression levels and blue indicates lower expression in PAs versus non-PAs. Differentially expressed genes were identified using the EdgeR package with adjusted p-value cutoffs <0.05 and log<sub>2</sub> fold changes > 2. (E) Independent validation of differential gene expression using mRNA isolated from PAs (EGFP<sup>+</sup>/DsRed<sup>+</sup>) and non-PAs (EGFP<sup>+</sup>/DsRed<sup>-</sup>). Note that the select genes analyzed show enrichment in PAs as compared to non-PAs, as revealed by qRT-PCR. Error bars indicate SE of the mean, n = 3. The red bars indicate EGFP<sup>+</sup>/DsRed<sup>+</sup> cell fractions. Expression differences between sorted cells were determined using two-way analysis of variance with Bonferroni post-hoc test, \*p<0.05, \*\*p<0.01, \*\*\*p<0.001, and \*\*\*\*p<0.0001.

<https://doi.org/10.1371/journal.pone.0240035.g005>

cells isolated from Mlc1-EGFP mice (Fig 6). Importantly, non-PAs did not segregate with the EGFP<sup>+</sup> cells. Lastly, we compared 10 PA-enriched genes identified and validated from the bulk RNAseq data, as well as 5 canonical astrocyte genes, with a published transcriptome dataset describing five sub-populations of astrocytes fractionated from three different brain regions based on differential expression of various cell surface markers [18]. As shown in S6 Fig, we detect some overlap in the expression of the PA-enriched genes with sub-sets of fractionated astrocytes, further supporting the PA identities of the fractionated cells from the Mlc1-EGFP mouse model. In summary, these various data reveal that we have isolated and transcriptionally profiled a new sub-population of astrocytes with likely roles in regulating brain vascular functions.

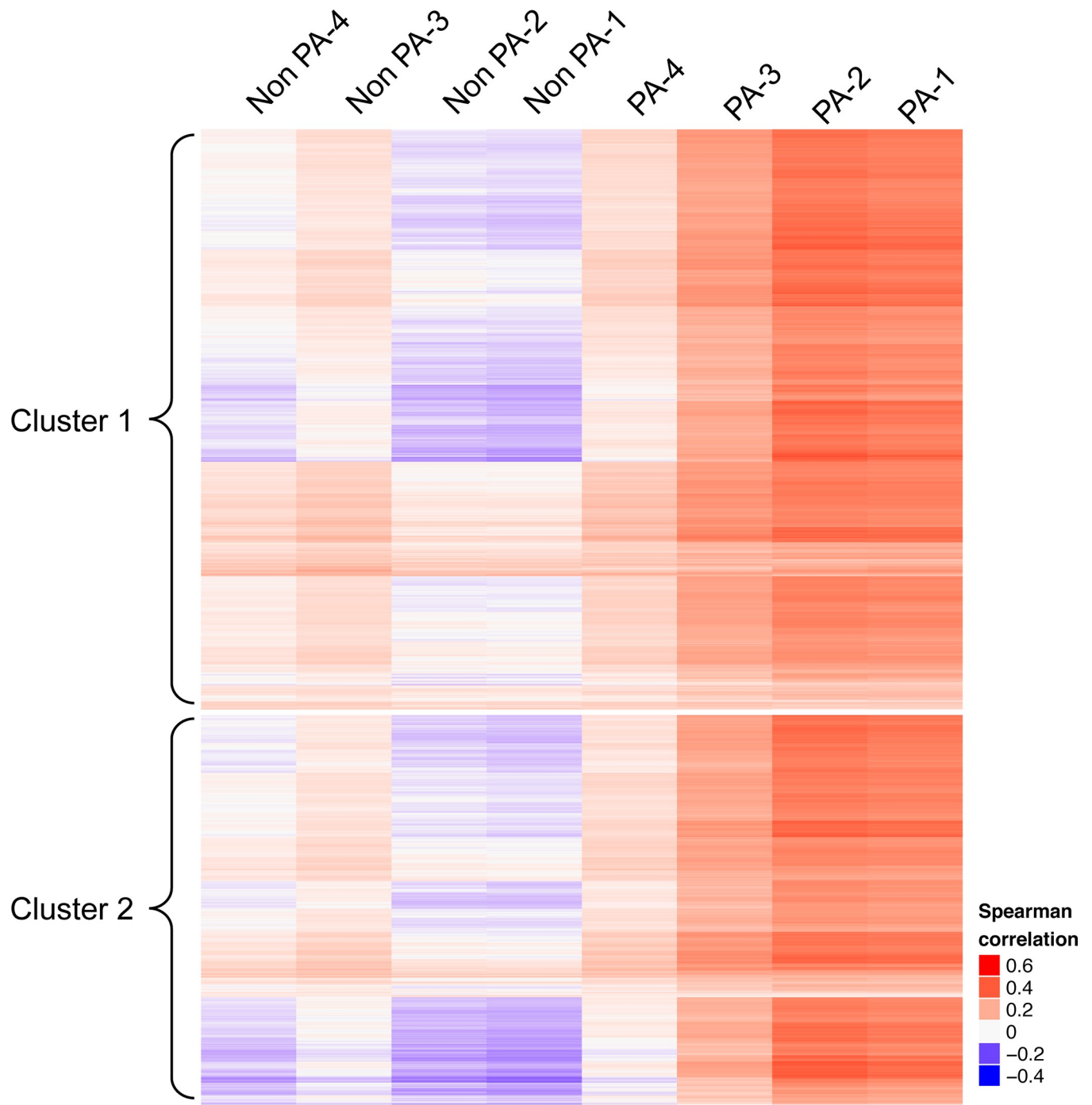


**Fig 6. Correlation analyses of bulk RNAseq and scRNAseq data.** Expression of genes in PAs (EGFP<sup>+</sup>) fractionated from Mlc1-EGFP mice and analyzed by single cell RNAseq (cell clusters 1 and 2, see Fig 2) were compared to gene expression patterns of PAs (EGFP<sup>+</sup>/DsRed<sup>+</sup>) and non-PAs (DsRed<sup>+</sup>) isolated from Mlc1-EGFP;GLAST-DsRed mice (n = 4). Note that gene expression patterns in purified PAs based on EGFP<sup>+</sup> or EGFP<sup>+</sup>/DsRed<sup>+</sup> expression correlate with each other, but do not correlate with non-PA expression patterns. Single cells from the scRNAseq analyses are shown along the y-axis. Heatmaps were colored using Pearson correlation coefficients between the gene expression of single cells in rows (y-axis) and expression of bulk samples (PA and non-PA samples) in columns (x-axis).

<https://doi.org/10.1371/journal.pone.0240035.g006>

## Discussion

In this report we have used genetically engineered mouse models, fluorescence-based cell fractionation, and quantitative RNA sequencing to identify several PA-expressed genes with putative links to vascular physiology. One central theme emerging from the data is that PA-enriched genes encode components linked to the ECM and cell adhesion. Prior studies of the brain vasculature revealed at least two different basement membranes (vascular endothelial and astrocyte) within the NVU [43]. PA-expressed ECM components identified from the RNAseq data include *Lama3*, which encodes the laminin  $\alpha 3$  component of laminin-332 [44] as well as *Lama5* which encodes the  $\alpha 5$  laminin subunit of laminin-511 [45]. These laminin subunits interact with other ECM proteins and have established roles in basement membrane biology in different organs. Loss-of-function mutations in human *LAMA3* gene are found in heritable forms of epidermolysis bullosa [46] and *Lama3* deletion in mice leads to similar skin blistering pathologies [47]. Laminin-511 in the vascular endothelial basement membrane is important for blood vessel integrity after experimentally-induced hemorrhagic stroke [48]. In this same study, roles for *Lama5* in BBB physiology in the healthy brain were not evident, possibly due to compensation by *Lama3* or other ECM proteins. It is possible that *Lama5* and *Lama3* expressed by PAs play key roles in NVU cytoarchitecture and BBB integrity under physiological settings. Interestingly, the RNAseq screen also identified the *Itga7* gene, which encodes  $\alpha 7$  integrin protein that dimerizes exclusively with  $\beta 1$  integrin. The integrin  $\alpha 7\beta 1$  is a receptor for laminins [49], with deletion of *Itga7* in mice leading to muscular dystrophy-like phenotypes due to defective adhesion and signaling pathways in skeletal muscle cells [50]. Some *Itga7*<sup>-/-</sup> mice develop vascular pathologies including cranial hemorrhage, which has been attributed to loss of  $\alpha 7\beta 1$  functions in vascular smooth muscle cells [51]. Our results suggest that  $\alpha 7\beta 1$  integrin in PAs is contributing additional roles in the vasculature, possibly via adhesion to laminin protein ligands in the astrocyte basement membrane. It will be interesting to determine if ablation of *Lama5/Lama3* or the *Itga7* genes in PAs impacts BBB permeability in physiological or pathological contexts. Along these lines, we are currently developing an Mlc1-CreERT2 knock-in mouse model for tamoxifen-inducible deletion of genes selectively in PAs.

In addition to laminins, the RNAseq experiments identified other ECM factors with roles in basement membrane integrity, including *Frem1* and *Frem2*. Mutations in *FREM1* or *FREM2* often result in human birth defects including congenital diaphragmatic hernia as well as abnormalities in craniofacial and renal development [52, 53]. The cell surface receptors for the Frem proteins have not been definitively identified [54]. It will be interesting to determine if  $\alpha 7\beta 1$  integrin is a receptor for these ECM proteins and whether there are interactions between the Frem proteins and laminins. PAs also selectively express various collagens, including *Col16a1*, *Col11a2*, and *Col4a5* as well as *P4ha2*, which encodes the alpha-2 subunit of prolyl 4-hydroxylase, a key enzyme involved in collagen synthesis and ECM deposition [55]. These results bolster our model for PA basement membrane control of blood vessel stability and BBB homeostasis.

PAs also express *Sema4a* and *Sema4b*, both members of the Semaphorin gene family that encode counter-receptors for plexins, neuropilins and some growth factor receptor tyrosine kinases [56]. Semaphorin 4a and 4b also have short cytoplasmic domains with likely signaling functions [57]. Phosphorylation of the Semaphorin 4b cytoplasmic domain has been shown to play important roles in reactive astrogliosis, with *Sema4b*<sup>-/-</sup> mice showing defects in the migration of reactive astrocytes to damaged regions following experimental brain injury [58]. PA expression of intracellular enzymes such as the kinase Alkp1, suggest that cell-intrinsic signaling pathways may control communication between PAs and vascular cells. Along these

lines, genetic deletion of *Alkp1* in mice leads to neurodegenerative phenotypes that may be due to BBB permeability defects [59]. Lastly, Mical-12/Jrab is a PA-enriched actin cytoskeleton adapter protein that promotes cell-cell junction formation in epithelial cells via transmembrane protein recycling through Rab GTPases [60, 61]. PAs also express *Als2cl*, which encodes a Rab GTPase exchange factor, suggesting that regulation of Rab activities via the Mical-12/Alsin pathway may control cell surface protein expression important for PA adhesion to the ECM.

The TGF $\beta$  superfamily member, *Gdf10*, was identified as a PA-enriched gene product. While glial-derived TGF $\beta$  signaling is important for angiogenesis and BBB formation during development [62], it remains uncertain if canonical TGF $\beta$  signaling in adult brain ECs is critical for BBB physiology. *Gdf10* is also expressed by adult brain ECs and promotes astrocyte and neuronal survival as well as BBB repair following stroke [63]. It will be important to determine if PA-derived Gdf10 protein is also playing a major role in blood vessel stability and BBB homeostasis in the healthy brain. Interestingly, we also identified *Prelp* as a gene enriched in PAs. *Prelp* encodes prolargin, a proline/arginine-rich end leucine-rich repeat protein and member of leucine rich repeat family of proteins that are expressed in ECM. Prior studies have shown that the related leucine rich repeat containing protein 33 is secreted into the brain microenvironment by microglia and promotes latent-TGF $\beta$  activation and signaling [64]. Hence, it will be important to determine if prolargin interacts with Gdf10 or other TGF $\beta$  family members to regulate PA adhesion and signaling functions. GSEA shows a Notch pathway signature involving several PA-expressed genes linked to the control of Notch processing, activation and transcriptional regulation. For example, *Lnfg* encodes a glycosyltransferase involved in Notch post-translational modification [65]. *Maml2* encodes mastermind 1, a Notch transcriptional regulatory factor [66]. How Notch signaling components may intersect with these events, as has been reported previously in studies of CNS angiogenesis [67], will be important to analyze. Links between these pathway components and Hedgehog signaling, which we also identified by GSEA as a signature pathway in PAs and has been reported previously to regulate BBB integrity and neuroinflammation [22], will also be interesting to study.

Abnormal control of BBB permeability is linked to the pathogenesis of various neurological diseases [68]. Many of the genes and pathways that are deregulated and contribute to neurovascular disease onset and progression remain largely unknown. It will be important to determine if deregulation of any of the PA-expressed genes we have identified in this study are altered in neurovascular-related brain disorders. Since mutations in *MLC1* cause the neurodevelopmental disorder MLC [69], it is possible that alterations in additional PA-expressed genes are linked to BBB defects in other pathologies. Lastly, there are human brain diseases, including various psychiatric disorders and age-related neurodegenerative pathologies, that develop without overt changes in BBB permeability. In these pathologies, the highly selective permeability properties of the BBB makes it a major impediment for delivering therapeutics [70]. Hence, there is a critical need to identify pathways that can be manipulated to allow reliable and effective delivery of drugs to the brain. Studying the PA-expressed genes identified in this study; therefore, will not only be informative for understanding the basic biology and pathophysiology of the NVU, but may also be potential targets for selectively modulating BBB permeability to enhance drug delivery to treat neurological diseases.

## Supporting information

**S1 Fig. Single cell RNAseq analysis in PAs isolated from adult Mlc1-EGFP mice.** Quantitative expression comparisons between the 7 different cell clusters identified by scRNAseq. Red indicates higher mRNA expression levels and blue indicates lower expression in EGFP-

expressing PAs. The differentially expressed genes were identified using the SEURAT package. (TIF)

**S2 Fig. Unbiased differential gene expression comparisons of PA clusters 1 and 2.** Unbiased expression comparisons of cell clusters 1 and 2 from scRNAseq reveal various differentially expressed genes. These data are based on adjusted p-value cutoff  $< 0.01$  (Wilcoxon rank-sum test) and log<sub>2</sub> fold change  $> 1$ . (TIF)

**S3 Fig. Comparative analysis of defined vascular and neural cell markers in isolated PAs.** Feature plots showing the expression of select mRNAs with established roles in vascular endothelial cells (*Cldn5* and *Pecam1*), pericytes (*Des* and *Acta2*), microglia (*Il1b* and *Tgfi*), neurons (*Trb1* and *Tubb3*), oligodendrocyte progenitor cells (*Pdgfra* and *Myrf*), and astroglial cells of the neurovascular unit (*Itgb8* and *Vegfa*) plotted by UMAP. Each dot indicates an RNA sequencing result from a different analyzed cell. Red indicates higher gene expression and grey indicates lower gene expression. Note that cell clusters one and two mainly show enrichment for the *Itgb8* and *Vegfa* mRNAs. The five other cell clusters do not show significant enrichment in the non-neurovascular markers. (TIF)

**S4 Fig. Gating controls for isolation of PAs from the adult mouse brain by FACS. (A-C);** Cerebral cortical cell suspensions from Mlc1-EGFP mice (A), GLAST-DsRed mice (B) or Mlc1-EGFP/GLAST-DsRed double-positive mice (C) were used for fractionation of EGFP<sup>+</sup> single positive or EGFP<sup>+</sup>/DsRed<sup>+</sup> double positive cells PAs or DsRed<sup>+</sup> single positive non-PAs. Single positive cells in panels A and B were used as gating controls for the double positive cell fractionation shown in panel C. (TIF)

**S5 Fig. Quantitative RNA sequencing to identify differentially expressed genes in PAs versus non-PAs isolated from Mlc1-EGFP;GLAST-DsRed adult mice.** Shown is a complete list of differentially expressed genes in PAs versus non-PAs as revealed by a color-coded heat map. The heat map includes the same samples shown in Fig 5C, but with all differentially expressed genes identified along the y-axis. The differentially expressed genes were identified using the EdgeR package with an adjusted p-value cutoff 0.05 and log<sub>2</sub> fold change  $> 2$ . (TIF)

**S6 Fig. Cross-referencing a 15 gene signature with published astrocyte transcriptome datasets.** Ten genes with enriched expression in PAs, and five canonical astrocyte genes (*Mlc1*, *Slc1a3*, *Gfap*, *Aldh1l1*, and *Itgb8*), were compared by hierarchical clustering to a published bulk RNAseq report (PMC5824716) involving five astrocyte sub-populations (termed A-E) isolated from three different brain regions (olfactory bulb, region 1; cortex, region 2; and brain stem, region 3). Note the partial overlap in expression between the PA-enriched genes and different astrocyte sub-populations in the published study. The individual genes in the 15 gene signature are shown in rows (y-axis) and the various sub-sets of astrocytes from different brain regions are shown in columns (x-axis). (TIF)

**S1 Table. Summary of commercial antibodies.**  
(DOCX)

**S2 Table. The 20 most enriched genes in cell cluster 1 from scRNAseq.**  
(DOCX)

**S3 Table. The 20 most enriched genes in cell cluster 2 from scRNAseq.**  
(DOCX)

**S4 Table. The 20 most enriched genes in cell cluster 3 from scRNAseq.**  
(DOCX)

**S5 Table. The 20 most enriched genes in cell cluster 4 from scRNAseq.**  
(DOCX)

**S6 Table. The 20 most enriched genes in cell cluster 5 from scRNAseq.**  
(DOCX)

**S7 Table. The 20 most enriched genes in cell cluster 6 from scRNAseq.**  
(DOCX)

**S8 Table. The 20 most enriched genes in cell cluster 7 from scRNAseq.**  
(DOCX)

**S9 Table. The top 10 signaling pathways in PAs as determined by Gene Set Enrichment Analyses (GSEA).**  
(DOCX)

**S10 Table. The top 30 genes with enriched expression in PAs versus non-PAs based on bulk RNAseq.**  
(DOCX)

**S11 Table.**  
(XLSX)

**S12 Table.**  
(XLSX)

## Acknowledgments

We thank Dr. Jing Wang in the Department of Bioinformatics and Computational Biology at MD Anderson Cancer Center for assistance with analysis and prioritization of the RNA sequencing data. We also thank the members of the McCarty laboratory for insightful comments on the manuscript.

## Author Contributions

**Conceptualization:** Nejla Yosef, Joseph H. McCarty.

**Data curation:** Nejla Yosef, Yuanxin Xi, Joseph H. McCarty.

**Formal analysis:** Nejla Yosef, Yuanxin Xi, Joseph H. McCarty.

**Funding acquisition:** Joseph H. McCarty.

**Investigation:** Joseph H. McCarty.

**Methodology:** Nejla Yosef, Yuanxin Xi, Joseph H. McCarty.

**Project administration:** Joseph H. McCarty.

**Writing – original draft:** Nejla Yosef, Joseph H. McCarty.

**Writing – review & editing:** Nejla Yosef, Yuanxin Xi, Joseph H. McCarty.

## References

1. Iadecola C. The Neurovascular Unit Coming of Age: A Journey through Neurovascular Coupling in Health and Disease. *Neuron*. 2017; 96(1):17–42. Epub 2017/09/29. <https://doi.org/10.1016/j.neuron.2017.07.030> PMID: 28957666; PubMed Central PMCID: PMC5657612.
2. Langen UH, Ayloo S, Gu C. Development and Cell Biology of the Blood-Brain Barrier. *Annu Rev Cell Dev Biol*. 2019; 35:591–613. Epub 2019/07/13. <https://doi.org/10.1146/annurev-cellbio-100617-062608> PMID: 31299172.
3. Paredes I, Himmels P, Ruiz de Almodovar C. Neurovascular Communication during CNS Development. *Dev Cell*. 2018; 45(1):10–32. <https://doi.org/10.1016/j.devcel.2018.01.023> PMID: 29634931.
4. Nakayama M, Nakayama A, van Lessen M, Yamamoto H, Hoffmann S, Drexler HC, et al. Spatial regulation of VEGF receptor endocytosis in angiogenesis. *Nat Cell Biol*. 2013; 15(3):249–60. Epub 2013/01/29. <https://doi.org/10.1038/ncb2679> PMID: 23354168; PubMed Central PMCID: PMC3901019.
5. Stenman JM, Rajagopal J, Carroll TJ, Ishibashi M, McMahon J, McMahon AP. Canonical Wnt signaling regulates organ-specific assembly and differentiation of CNS vasculature. *Science*. 2008; 322(5905):1247–50. <https://doi.org/10.1126/science.1164594> PMID: 19023080.
6. Liebner S, Corada M, Bangsow T, Babbage J, Taddei A, Czupalla CJ, et al. Wnt/beta-catenin signaling controls development of the blood-brain barrier. *J Cell Biol*. 2008; 183(3):409–17. <https://doi.org/10.1083/jcb.200806024> PMID: 18955553.
7. Kuhnert F, Mancuso MR, Shamloo A, Wang HT, Choksi V, Florek M, et al. Essential regulation of CNS angiogenesis by the orphan G protein-coupled receptor GPR124. *Science*. 2010; 330(6006):985–9. <https://doi.org/10.1126/science.1196554> PMID: 21071672; PubMed Central PMCID: PMC3099479.
8. Posokhova E, Shukla A, Seaman S, Volate S, Hilton MB, Wu B, et al. GPR124 functions as a WNT7-specific coactivator of canonical beta-catenin signaling. *Cell Rep*. 2015; 10(2):123–30. <https://doi.org/10.1016/j.celrep.2014.12.020> PMID: 25558062; PubMed Central PMCID: PMC4331012.
9. Vanhollenbeke B, Stone OA, Bostaille N, Cho C, Zhou Y, Maquet E, et al. Tip cell-specific requirement for an atypical Gpr124- and Reck-dependent Wnt/beta-catenin pathway during brain angiogenesis. *Elife*. 2015; 4. <https://doi.org/10.7554/eLife.06489> PMID: 26051822; PubMed Central PMCID: PMC4456509.
10. Arnold TD, Niaudet C, Pang MF, Siegenthaler J, Gaengel K, Jung B, et al. Excessive vascular sprouting underlies cerebral hemorrhage in mice lacking alphaVbeta8-TGFbeta signaling in the brain. *Development*. 2014; 141(23):4489–99. <https://doi.org/10.1242/dev.107193> PMID: 25406396; PubMed Central PMCID: PMC4302931.
11. Hirota S, Clements TP, Tang LK, Morales JE, Lee HS, Oh SP, et al. Neuropilin 1 balances beta8 integrin-activated TGFbeta signaling to control sprouting angiogenesis in the brain. *Development*. 2015; 142(24):4363–73. <https://doi.org/10.1242/dev.113746> PMID: 26586223; PubMed Central PMCID: PMC4689212.
12. Hirota S, Liu Q, Lee HS, Hossain MG, Lacy-Hulbert A, McCarty JH. The astrocyte-expressed integrin alphaVbeta8 governs blood vessel sprouting in the developing retina. *Development*. 2011; 138(23):5157–66. <https://doi.org/10.1242/dev.069153> PMID: 22069187; PubMed Central PMCID: PMC3253036.
13. Ma S, Santhosh D, Kumar TP, Huang Z. A Brain-Region-Specific Neural Pathway Regulating Germinal Matrix Angiogenesis. *Dev Cell*. 2017; 41(4):366–81 e4. <https://doi.org/10.1016/j.devcel.2017.04.014> PMID: 28535372; PubMed Central PMCID: PMC5492999.
14. Abbott NJ, Ronnback L, Hansson E. Astrocyte-endothelial interactions at the blood-brain barrier. *Nat Rev Neurosci*. 2006; 7(1):41–53. Epub 2005/12/24. <https://doi.org/10.1038/nrn1824> PMID: 16371949.
15. Daneman R, Prat A. The blood-brain barrier. *Cold Spring Harb Perspect Biol*. 2015; 7(1):a020412. Epub 2015/01/07. <https://doi.org/10.1101/cshperspect.a020412> PMID: 25561720; PubMed Central PMCID: PMC4292164.
16. Lien CF, Mohanta SK, Frontczak-Baniewicz M, Swinny JD, Zablocka B, Gorecki DC. Absence of glial alpha-dystrobrevin causes abnormalities of the blood-brain barrier and progressive brain edema. *J Biol Chem*. 2012; 287(49):41374–85. Epub 2012/10/09. <https://doi.org/10.1074/jbc.M112.400044> PMID: 23043099; PubMed Central PMCID: PMC3510835.
17. Chai H, Diaz-Castro B, Shigetomi E, Monte E, Oceau JC, Yu X, et al. Neural Circuit-Specialized Astrocytes: Transcriptomic, Proteomic, Morphological, and Functional Evidence. *Neuron*. 2017; 95(3):531–49 e9. Epub 2017/07/18. <https://doi.org/10.1016/j.neuron.2017.06.029> PMID: 28712653; PubMed Central PMCID: PMC5811312.
18. John Lin CC, Yu K, Hatcher A, Huang TW, Lee HK, Carlson J, et al. Identification of diverse astrocyte populations and their malignant analogs. *Nat Neurosci*. 2017; 20(3):396–405. Epub 2017/02/07. <https://doi.org/10.1038/nn.4493> PMID: 28166219; PubMed Central PMCID: PMC5824716.

19. Waite A, Brown SC, Blake DJ. The dystrophin-glycoprotein complex in brain development and disease. *Trends Neurosci.* 2012; 35(8):487–96. Epub 2012/05/26. <https://doi.org/10.1016/j.tins.2012.04.004> PMID: 22626542.
20. Bragg AD, Das SS, Froehner SC. Dystrophin-associated protein scaffolding in brain requires alpha-dystrobrevin. *Neuroreport.* 2010; 21(10):695–9. Epub 2010/05/29. <https://doi.org/10.1097/WNR.0b013e32833b0a3b> PMID: 20508543; PubMed Central PMCID: PMC2889226.
21. Zhou J, Kong H, Hua X, Xiao M, Ding J, Hu G. Altered blood-brain barrier integrity in adult aquaporin-4 knockout mice. *Neuroreport.* 2008; 19(1):1–5. Epub 2008/02/19. <https://doi.org/10.1097/WNR.0b013e3282f2b4eb> PMID: 18281883.
22. Alvarez JI, Dodelet-Devillers A, Kebir H, Ifergan I, Fabre PJ, Terouz S, et al. The Hedgehog pathway promotes blood-brain barrier integrity and CNS immune quiescence. *Science.* 2011; 334(6063):1727–31. Epub 2011/12/07. <https://doi.org/10.1126/science.1206936> PMID: 22144466.
23. Tiwary S, Morales JE, Kwiatkowski SC, Lang FF, Rao G, McCarty JH. Metastatic Brain Tumors Disrupt the Blood-Brain Barrier and Alter Lipid Metabolism by Inhibiting Expression of the Endothelial Cell Fatty Acid Transporter Mfsd2a. *Sci Rep.* 2018; 8(1):8267. Epub 2018/05/31. <https://doi.org/10.1038/s41598-018-26636-6> PMID: 29844613; PubMed Central PMCID: PMC5974340.
24. Ben-Zvi A, Lacoste B, Kur E, Andreone BJ, Mayshar Y, Yan H, et al. Mfsd2a is critical for the formation and function of the blood-brain barrier. *Nature.* 2014; 509(7501):507–11. <https://doi.org/10.1038/nature13324> PMID: 24828040; PubMed Central PMCID: PMC4134871.
25. Nguyen LN, Ma D, Shui G, Wong P, Cazenave-Gassiot A, Zhang X, et al. Mfsd2a is a transporter for the essential omega-3 fatty acid docosahexaenoic acid. *Nature.* 2014; 509(7501):503–6. <https://doi.org/10.1038/nature13241> PMID: 24828044.
26. Guemez-Gamboa A, Nguyen LN, Yang H, Zaki MS, Kara M, Ben-Omran T, et al. Inactivating mutations in MFSD2A, required for omega-3 fatty acid transport in brain, cause a lethal microcephaly syndrome. *Nat Genet.* 2015; 47(7):809–13. <https://doi.org/10.1038/ng.3311> PMID: 26005868; PubMed Central PMCID: PMC4547531.
27. Mishra A, Reynolds JP, Chen Y, Gourine AV, Rusakov DA, Attwell D. Astrocytes mediate neurovascular signaling to capillary pericytes but not to arterioles. *Nat Neurosci.* 2016; 19(12):1619–27. Epub 2016/11/01. <https://doi.org/10.1038/nn.4428> PMID: 27775719; PubMed Central PMCID: PMC5131849.
28. Sweeney MD, Ayyadurai S, Zlokovic BV. Pericytes of the neurovascular unit: key functions and signaling pathways. *Nat Neurosci.* 2016; 19(6):771–83. Epub 2016/05/27. <https://doi.org/10.1038/nn.4288> PMID: 27227366; PubMed Central PMCID: PMC5745011.
29. Iliff JJ, Wang M, Liao Y, Plogg BA, Peng W, Gundersen GA, et al. A paravascular pathway facilitates CSF flow through the brain parenchyma and the clearance of interstitial solutes, including amyloid beta. *Sci Transl Med.* 2012; 4(147):147ra11. Epub 2012/08/17. <https://doi.org/10.1126/scitranslmed.3003748> PMID: 22896675; PubMed Central PMCID: PMC3551275.
30. Guo D, Zou J, Rensing N, Wong M. In Vivo Two-Photon Imaging of Astrocytes in GFAP-GFP Transgenic Mice. *PLoS One.* 2017; 12(1):e0170005. Epub 2017/01/21. <https://doi.org/10.1371/journal.pone.0170005> PMID: 28107381; PubMed Central PMCID: PMC5249218.
31. Oceau JC, Chai H, Jiang R, Bonanno SL, Martin KC, Khakh BS. An Optical Neuron-Astrocyte Proximity Assay at Synaptic Distance Scales. *Neuron.* 2018; 98(1):49–66 e9. Epub 2018/04/06. <https://doi.org/10.1016/j.neuron.2018.03.003> PMID: 29621490; PubMed Central PMCID: PMC5916847.
32. Heng JS, Rattner A, Stein-O'Brien GL, Winer BL, Jones BW, Vernon HJ, et al. Hypoxia tolerance in the Norrin-deficient retina and the chronically hypoxic brain studied at single-cell resolution. *Proc Natl Acad Sci U S A.* 2019; 116(18):9103–14. Epub 2019/04/17. <https://doi.org/10.1073/pnas.1821122116> PMID: 30988181; PubMed Central PMCID: PMC6500147.
33. Boor PK, de Groot K, Waisfisz Q, Kamphorst W, Oudejans CB, Powers JM, et al. MLC1: a novel protein in distal astroglial processes. *J Neuropathol Exp Neurol.* 2005; 64(5):412–9. Epub 2005/05/17. <https://doi.org/10.1093/jnen/64.5.412> PMID: 15892299.
34. Toutouchian JJ, McCarty JH. Selective expression of eGFP in mouse perivascular astrocytes by modification of the Mlc1 gene using T2A-based ribosome skipping. *Genesis.* 2017; 55(10). Epub 2017/09/21. <https://doi.org/10.1002/dvg.23071> PMID: 28929580; PubMed Central PMCID: PMC5771503.
35. Regan MR, Huang YH, Kim YS, Dykes-Hoberg MI, Jin L, Watkins AM, et al. Variations in promoter activity reveal a differential expression and physiology of glutamate transporters by glia in the developing and mature CNS. *J Neurosci.* 2007; 27(25):6607–19. Epub 2007/06/22. <https://doi.org/10.1523/JNEUROSCI.0790-07.2007> PMID: 17581948; PubMed Central PMCID: PMC6672708.
36. Jamieson AR, Giger ML, Drukker K, Li H, Yuan Y, Bhooshan N. Exploring nonlinear feature space dimension reduction and data representation in breast Cadx with Laplacian eigenmaps and t-SNE. *Med Phys.* 2010; 37(1):339–51. Epub 2010/02/24. <https://doi.org/10.1118/1.3267037> PMID: 20175497; PubMed Central PMCID: PMC2807447.



37. Kim D, Pertea G, Trapnell C, Pimentel H, Kelley R, Salzberg SL. TopHat2: accurate alignment of transcriptomes in the presence of insertions, deletions and gene fusions. *Genome Biol.* 2013; 14(4):R36. Epub 2013/04/27. <https://doi.org/10.1186/gb-2013-14-4-r36> PMID: 23618408; PubMed Central PMCID: PMC4053844.
38. Anders S, Pyl PT, Huber W. HTSeq—a Python framework to work with high-throughput sequencing data. *Bioinformatics.* 2015; 31(2):166–9. Epub 2014/09/28. <https://doi.org/10.1093/bioinformatics/btu638> PMID: 25260700; PubMed Central PMCID: PMC4287950.
39. Robinson MD, McCarthy DJ, Smyth GK. edgeR: a Bioconductor package for differential expression analysis of digital gene expression data. *Bioinformatics.* 2010; 26(1):139–40. Epub 2009/11/17. <https://doi.org/10.1093/bioinformatics/btp616> PMID: 19910308; PubMed Central PMCID: PMC2796818.
40. Subramanian A, Tamayo P, Mootha VK, Mukherjee S, Ebert BL, Gillette MA, et al. Gene set enrichment analysis: a knowledge-based approach for interpreting genome-wide expression profiles. *Proc Natl Acad Sci U S A.* 2005; 102(43):15545–50. Epub 2005/10/04. <https://doi.org/10.1073/pnas.0506580102> PMID: 16199517; PubMed Central PMCID: PMC1239896.
41. McCarty JH. alphavbeta8 integrin adhesion and signaling pathways in development, physiology and disease. *J Cell Sci.* 2020; 133(12). Epub 2020/06/17. <https://doi.org/10.1242/jcs.239434> PMID: 32540905.
42. Paul R, Zhang ZG, Eliceiri BP, Jiang Q, Boccia AD, Zhang RL, et al. Src deficiency or blockade of Src activity in mice provides cerebral protection following stroke. *Nat Med.* 2001; 7(2):222–7. Epub 2001/02/15. <https://doi.org/10.1038/84675> PMID: 11175854.
43. Sixt M, Engelhardt B, Pausch F, Hallmann R, Wendler O, Sorokin LM. Endothelial cell laminin isoforms, laminins 8 and 10, play decisive roles in T cell recruitment across the blood-brain barrier in experimental autoimmune encephalomyelitis. *J Cell Biol.* 2001; 153(5):933–46. Epub 2001/05/31. <https://doi.org/10.1083/jcb.153.5.933> PMID: 11381080; PubMed Central PMCID: PMC2174323.
44. Rousselle P, Beck K. Laminin 332 processing impacts cellular behavior. *Cell Adh Migr.* 2013; 7(1):122–34. Epub 2012/12/25. <https://doi.org/10.4161/cam.23132> PMID: 23263634; PubMed Central PMCID: PMC3544776.
45. Pouliot N, Kusuma N. Laminin-511: a multi-functional adhesion protein regulating cell migration, tumor invasion and metastasis. *Cell Adh Migr.* 2013; 7(1):142–9. Epub 2012/10/19. <https://doi.org/10.4161/cam.22125> PMID: 23076212; PubMed Central PMCID: PMC3544778.
46. Muhle C, Schneider H. Novel human pathological mutations. Gene symbol: LAMA3. Disease: junctional epidermolysis bullosa. *Hum Genet.* 2007; 122(5):549. Epub 2008/04/02. PMID: 18380027.
47. Pesch M, Konig S, Aumailley M. Targeted Disruption of the Lama3 Gene in Adult Mice Is Sufficient to Induce Skin Inflammation and Fibrosis. *J Invest Dermatol.* 2017; 137(2):332–40. Epub 2016/10/13. <https://doi.org/10.1016/j.jid.2016.07.040> PMID: 27729280.
48. Gautam J, Miner JH, Yao Y. Loss of Endothelial Laminin alpha5 Exacerbates Hemorrhagic Brain Injury. *Transl Stroke Res.* 2019; 10(6):705–18. Epub 2019/01/30. <https://doi.org/10.1007/s12975-019-0688-5> PMID: 30693425; PubMed Central PMCID: PMC6663661.
49. Kobayashi N, Oda T, Takizawa M, Ishizaki T, Tsukamoto N, Yokohama A, et al. Integrin alpha7 and Extracellular Matrix Laminin 211 Interaction Promotes Proliferation of Acute Myeloid Leukemia Cells and Is Associated with Granulocytic Sarcoma. *Cancers (Basel).* 2020; 12(2). Epub 2020/02/09. <https://doi.org/10.3390/cancers12020363> PMID: 32033262; PubMed Central PMCID: PMC7072541.
50. Mayer U, Saher G, Fassler R, Bornemann A, Echtermeyer F, von der Mark H, et al. Absence of integrin alpha 7 causes a novel form of muscular dystrophy. *Nat Genet.* 1997; 17(3):318–23. Epub 1997/11/14. <https://doi.org/10.1038/ng1197-318> PMID: 9354797.
51. Flintoff-Dye NL, Welsler J, Rooney J, Scowen P, Tamowski S, Hatton W, et al. Role for the alpha7beta1 integrin in vascular development and integrity. *Dev Dyn.* 2005; 234(1):11–21. Epub 2005/07/09. <https://doi.org/10.1002/dvdy.20462> PMID: 16003770.
52. Beck TF, Veenma D, Shchelochkov OA, Yu Z, Kim BJ, Zaveri HP, et al. Deficiency of FRAS1-related extracellular matrix 1 (FREM1) causes congenital diaphragmatic hernia in humans and mice. *Hum Mol Genet.* 2013; 22(5):1026–38. Epub 2012/12/12. <https://doi.org/10.1093/hmg/dds507> PMID: 23221805; PubMed Central PMCID: PMC3561915.
53. Nathanson J, Swarr DT, Singer A, Liu M, Chinn A, Jones W, et al. Novel FREM1 mutations expand the phenotypic spectrum associated with Manitoba-oculo-tricho-anal (MOTA) syndrome and bifid nose renal agenesis anorectal malformations (BNAR) syndrome. *Am J Med Genet A.* 2013; 161A(3):473–8. Epub 2013/02/13. <https://doi.org/10.1002/ajmg.a.35736> PMID: 23401257; PubMed Central PMCID: PMC3581754.
54. Pavlakis E, Chiotaki R, Chalepakis G. The role of Fras1/Frem proteins in the structure and function of basement membrane. *Int J Biochem Cell Biol.* 2011; 43(4):487–95. Epub 2010/12/25. <https://doi.org/10.1016/j.biocel.2010.12.016> PMID: 21182980.

55. Grimmer C, Balbus N, Lang U, Aigner T, Cramer T, Muller L, et al. Regulation of type II collagen synthesis during osteoarthritis by prolyl-4-hydroxylases: possible influence of low oxygen levels. *Am J Pathol*. 2006; 169(2):491–502. Epub 2006/08/01. <https://doi.org/10.2353/ajpath.2006.050738> PMID: 16877351; PubMed Central PMCID: PMC1698781.
56. Hu S, Zhu L. Semaphorins and Their Receptors: From Axonal Guidance to Atherosclerosis. *Front Physiol*. 2018; 9:1236. Epub 2018/11/09. <https://doi.org/10.3389/fphys.2018.01236> PMID: 30405423; PubMed Central PMCID: PMC6196129.
57. Alto LT, Terman JR. Semaphorins and their Signaling Mechanisms. *Methods Mol Biol*. 2017; 1493:1–25. Epub 2016/10/28. [https://doi.org/10.1007/978-1-4939-6448-2\\_1](https://doi.org/10.1007/978-1-4939-6448-2_1) PMID: 27787839; PubMed Central PMCID: PMC5538787.
58. Ben-Gigi L, Sweetat S, Besser E, Fellig Y, Wiederhold T, Polakiewicz RD, et al. Astroglialosis Induced by Brain Injury Is Regulated by Sema4B Phosphorylation. *eNeuro*. 2015; 2(3). Epub 2015/10/16. <https://doi.org/10.1523/ENEURO.0078-14.2015> PMID: 26464987; PubMed Central PMCID: PMC4586933.
59. Chen M, Xu R. Motor coordination deficits in *Alpk1* mutant mice with the inserted piggyBac transposon. *BMC Neurosci*. 2011; 12:1. Epub 2011/01/07. <https://doi.org/10.1186/1471-2202-12-1> PMID: 21208416; PubMed Central PMCID: PMC3030534.
60. Sakane A, Abdallah AA, Nakano K, Honda K, Ikeda W, Nishikawa Y, et al. Rab13 small G protein and junctional Rab13-binding protein (JRAB) orchestrate actin cytoskeletal organization during epithelial junctional development. *J Biol Chem*. 2012; 287(51):42455–68. Epub 2012/10/27. <https://doi.org/10.1074/jbc.M112.383653> PMID: 23100251; PubMed Central PMCID: PMC3522248.
61. Sakane A, Honda K, Sasaki T. Rab13 regulates neurite outgrowth in PC12 cells through its effector protein, JRAB/MICAL-L2. *Mol Cell Biol*. 2010; 30(4):1077–87. Epub 2009/12/17. <https://doi.org/10.1128/MCB.01067-09> PMID: 20008558; PubMed Central PMCID: PMC2815571.
62. Kofler N, Simons M. The expanding role of neuropilin: regulation of transforming growth factor-beta and platelet-derived growth factor signaling in the vasculature. *Curr Opin Hematol*. 2016; 23(3):260–7. Epub 2016/02/06. <https://doi.org/10.1097/MOH.0000000000000233> PMID: 26849476; PubMed Central PMCID: PMC4957701.
63. Li S, Nie EH, Yin Y, Benowitz LI, Tung S, Vinters HV, et al. GDF10 is a signal for axonal sprouting and functional recovery after stroke. *Nat Neurosci*. 2015; 18(12):1737–45. Epub 2015/10/27. <https://doi.org/10.1038/nn.4146> PMID: 26502261; PubMed Central PMCID: PMC4790086.
64. Qin Y, Garrison BS, Ma W, Wang R, Jiang A, Li J, et al. A Milieu Molecule for TGF-beta Required for Microglia Function in the Nervous System. *Cell*. 2018; 174(1):156–71 e16. <https://doi.org/10.1016/j.cell.2018.05.027> PMID: 29909984; PubMed Central PMCID: PMC6089614.
65. Urata Y, Takeuchi H. Effects of Notch glycosylation on health and diseases. *Dev Growth Differ*. 2020; 62(1):35–48. Epub 2019/12/31. <https://doi.org/10.1111/dgd.12643> PMID: 31886522.
66. Kitagawa M. Notch signalling in the nucleus: roles of Mastermind-like (MAML) transcriptional coactivators. *J Biochem*. 2016; 159(3):287–94. Epub 2015/12/30. <https://doi.org/10.1093/jb/mvv123> PMID: 26711237.
67. Aspalter IM, Gordon E, Dubrac A, Ragab A, Narloch J, Vizan P, et al. *Alk1* and *Alk5* inhibition by *Nrp1* controls vascular sprouting downstream of Notch. *Nat Commun*. 2015; 6:7264. Epub 2015/06/18. <https://doi.org/10.1038/ncomms8264> PMID: 26081042; PubMed Central PMCID: PMC4557308.
68. Sweeney MD, Zhao Z, Montagne A, Nelson AR, Zlokovic BV. Blood-Brain Barrier: From Physiology to Disease and Back. *Physiol Rev*. 2019; 99(1):21–78. Epub 2018/10/04. <https://doi.org/10.1152/physrev.00050.2017> PMID: 30280653; PubMed Central PMCID: PMC6335099.
69. van der Knaap MS, Boor I, Estevez R. Megalencephalic leukoencephalopathy with subcortical cysts: chronic white matter oedema due to a defect in brain ion and water homeostasis. *Lancet Neurol*. 2012; 11(11):973–85. Epub 2012/10/20. [https://doi.org/10.1016/S1474-4422\(12\)70192-8](https://doi.org/10.1016/S1474-4422(12)70192-8) PMID: 23079554.
70. Umlauf BJ, Shusta EV. Exploiting BBB disruption for the delivery of nanocarriers to the diseased CNS. *Curr Opin Biotechnol*. 2019; 60:146–52. Epub 2019/03/09. <https://doi.org/10.1016/j.copbio.2019.01.013> PMID: 30849699; PubMed Central PMCID: PMC6728237.